



1

2

3

4

5

6

7

8

9

10 Amélie Simon\*<sup>1 2</sup>, Guillaume Gastineau<sup>1</sup>, Claude Frankignoul<sup>1</sup>,  
11 Vladimir Lapin <sup>3</sup>, Pablo Ortega <sup>3</sup>

12

13 <sup>1</sup> UMR LOCEAN, Sorbonne Université/IRD/MNHN/CNRS, Paris,  
14 France

15 <sup>2</sup> Instituto Dom Luiz (IDL), Faculdade de Ciências, Universidade  
16 de Lisboa, Lisboa, Portugal.

17 <sup>3</sup> Barcelona Supercomputing Center, Barcelona, Spain

18

19 \*Corresponding author address: [ajsimon@fc.ul.pt](mailto:ajsimon@fc.ul.pt)

20

21

22

23

1

2



## Abstract

24

25

26 The modulation of the winter impacts of Arctic sea ice loss by the Pacific Decadal Oscillation  
27 (PDO) is investigated in the IPSL-CM6A-LR ocean-atmosphere general circulation model.  
28 Ensembles of simulations are performed with constrained sea ice concentration corresponding  
29 to pre-industrial, present-day and future states, and initial conditions sampling warm and cold  
30 phases of the PDO. Using a general linear model, we estimate the simulated winter impact of  
31 sea ice loss, PDO and their combined effects. In response to sea ice loss, the Arctic lower  
32 troposphere warms and a negative North-Atlantic oscillation like pattern appears together with a  
33 weak deepening of the Aleutian Low. The two patterns are associated with a weakening of the  
34 poleward flank of the eddy-driven jet, while in the stratospheric the polar vortex weakens.  
35 Besides, a warm PDO phase induces a large positive Pacific North America pattern, as well as  
36 a small negative Arctic oscillation pattern associated with a weakening of the stratospheric polar  
37 vortex. However, the effects of PDO and Arctic sea ice loss are not additive. The Arctic sea ice  
38 teleconnections in both troposphere and stratosphere are reduced by the PDO, most  
39 importantly in the stratosphere. The results are discussed and compared to those obtained with  
40 the same model in atmosphere-only simulations, where sea ice loss does not significantly alter  
41 the stratospheric polar vortex.

42

43

44

45

46

47

48

49

50

51

52

53

54

55

56

57

58

59

60

61

62

63

64

3

4



## Introduction

65

66

67 Since the late 1970s, the Arctic sea ice extent has exhibited a significant decline in all seasons,  
68 which is due to human influence (IPCC, 2021 report: Masson-Delmotte et al., 2021) and is  
69 expected to continue. Climate models project a summer ice-free Arctic Ocean by 2050, although  
70 this date varies depending on the climate scenario considered (SIMIP Community, 2020). Many  
71 studies have shown that the Arctic sea ice loss is likely to change the mid-latitude climate, but  
72 its extent is still a matter of debate (Cohen et al., 2014; Blackport and Screen, 2020).

73

74 Studies with observations have linked the loss of Arctic sea ice in late fall to a negative North  
75 Atlantic Oscillation (NAO) in winter (King et al., 2016; Garcia-Serrano et al., 2015; Simon et al.  
76 2020). However, there are many confounding factors at play and the observational period is too  
77 short to accurately assess the amplitude of the sea ice loss impact. On the one hand, most  
78 atmospheric models forced by a reduction of Arctic sea ice cover simulate a negative NAO-type  
79 response in winter (Sun et al., 2015; Peings and Magnusdottir, 2014; Liang et al., 2021; Levine  
80 et al. 2021; Smith et al., 2022). Nevertheless, this result is not completely robust as some  
81 studies reported a positive NAO (Screen et al., 2014; Cassano et al., 2014) or a weak response  
82 that does not project onto the NAO (Screen et al., 2013; Blackport and Kushner, 2016; Dai and  
83 Song, 2020). Some of the differences across models can be explained by different regional  
84 expressions of Arctic sea ice loss (Levine et al., 2021). On the other hand, all coupled models  
85 show a negative NAO response (Deser et al., 2015; Screen et al., 2018; Simon et al., 2021) but  
86 fewer studies exist. Furthermore, when comparing observational and modeling studies, the  
87 amplitude of the negative NAO response is much weaker for models than in observations (Liang  
88 et al., 2021). Understanding these differences within models and between models and  
89 observations is an active topic of research (Cohen et al, 2020). For instance, among the  
90 coupled model studies, there are very contrasting impacts of the sea ice loss on the Aleutian  
91 low. Screen et al. (2018) found a strengthening of the Aleutian low in six sensitivity experiments  
92 involving different models or methodologies to melt the sea ice while Cvijanovic et al. (2017),  
93 Simon et al. (2021) and Seidenglanz et al. (2021) found a weakening of the Aleutian low or a  
94 ridge in the North Pacific, and Blackport and Screen (2019) found no clear Aleutian Low  
95 response. A weakening of the Aleutian low in late winter has been associated with less vertical  
96 propagation of planetary waves into the stratosphere and to an acceleration of the polar vortex  
97 (Nakamura and Honda, 2002; Garfinkel et al., 2010; Smith et al., 2010). Therefore, whether the  
98 Arctic sea ice loss affects the polar vortex is still an open question (Cohen et al., 2020). Indeed,  
99 some studies found a weakening of the polar vortex in response to Arctic sea ice loss (Kim et  
100 al., 2014; Peings & Magnusdottir, 2014; King et al., 2016; Kretschmer et al., 2016; Screen,  
101 2017; Zhang et al., 2016; Hoshi et al.; 2019) while others found no robust winter stratospheric  
102 circulation response (Smith et al., 2022). A lack of stratospheric polar vortex changes could be  
103 potentially related to canceling effects from sea ice loss in the Atlantic and Pacific sectors (Sun  
104 et al., 2015).

105

106 The various responses to Arctic sea ice loss among the previous studies suggest that there  
107 might be concomitant signals that interfere with the Arctic sea ice loss impacts (Ogawa et al.,

5

6

3



108 2018). Labe et al. (2019) found that for melting sea ice, December Wave 1 components of the  
109 300 hPa geopotential height were reinforced under the East phase of the Quasi-Biennial  
110 Oscillation. Gastineau et al. (2017) and Simon et al. (2020) using multivariate regressions found  
111 that early winter snow cover in Eurasia and sea ice in the Arctic could constructively interfere to  
112 weaken the polar vortex. Peings et al. (2019) and Blackport and Screen (2020) showed that  
113 Ural Blocking can more effectively drive a weakening of the polar vortex than a concomitant sea  
114 ice reduction. Arctic-midlatitude linkages may also be affected by sea surface temperature  
115 (SST) variability, as discussed by Ogawa et al. (2018), Cohen et al. (2020), Dai and Song  
116 (2020) and Simon et al. (2020). The Atlantic Multidecadal Variability (AMV) could regulate the  
117 Arctic sea ice loss impact on Arctic Oscillation (AO)-like through the stratospheric pathway (Li et  
118 al., 2018) or on Pacific-North America atmospheric circulation through horizontal wave  
119 propagation (Osborne et al., 2017). Liang et al. (2021) showed that the North Atlantic horseshoe  
120 SST pattern (Czaja and Frankignoul, 1999; 2002) and Arctic sea ice concentration act  
121 oppositely on the atmosphere in late winter. Also, Park et al. (2016) revealed that the North  
122 Pacific SST could modulate the effect of the Arctic Oscillation on winter temperature in East  
123 Asia. Using a composite analysis, Screen and Francis (2016) investigated observations and  
124 atmospheric model simulations forced with different Pacific Decadal Oscillation (PDO; Mantua  
125 et al., 1997) patterns and sea ice extensions. They found that during the warm phase of the  
126 PDO, the contribution of sea ice loss to Arctic amplification was smaller than during the cold  
127 PDO phase. Many of the model results discussed above are based on individual models, a  
128 small selection of models, and/or use one particular methodology. It's therefore essential to  
129 extend the analyses to other models or new methodological approaches.

130

131 In the present paper, we focus in particular on how persistent PDO-like SST anomalies could  
132 modulate the influence of Arctic sea ice loss on the Northern Hemisphere atmospheric  
133 circulation. We will be revisiting the previous results of Screen and Francis (2016) with the  
134 novelty to account for atmospheric-ocean feedback using a coupled model and under the light  
135 of a new method based on general linear models to assess the interaction between sea ice loss  
136 and the PDO. The results agree with Screen and Francis (2016) in that the sea ice loss induces  
137 a weakening of PDO teleconnections. In addition, the presented method allows accurate  
138 quantification of the interactions.

139

140

## 141 Methodology

142

143

144 We use the Institut Pierre Simon Laplace coupled model (IPSL-CM6A-LR; Boucher et al., 2020)  
145 which contributed to the 6th phase of the international Coupled Model Intercomparison Project  
146 (CMIP6; Eyring et al., 2016). The IPSL-CM6-LR uses the atmospheric component LMDZ6A  
147 (Hourdin et al., 2020) which includes the land model ORCHIDEE version 2 (Cheruy et al.,  
148 2020). It has a 79-layer vertical discretization ranging from about 10 m to 80 km above surface  
149 (top at 1 Pa) and a horizontal resolution of  $144 \times 143$  points ( $2.5^\circ$  in longitude and  $1.25^\circ$  in  
150 latitude). The ocean component is the Version 3.6 stable of NEMO (Nucleus for European  
Models of the Ocean), which includes the ocean physics module OPA (Madec et al., 2017), the

7



151 sea ice dynamics and thermodynamics module LIM3 (Vancoppenolle et al., 2009; Rousset et  
152 al., 2015), and the ocean biogeochemistry module PISCES (Aumont et al., 2015). All NEMO  
153 components share the same tripolar grid, eORCA1xL75, with a horizontal resolution of about 1°  
154 except in the tropics where the latitudinal resolution decreases to 1/2°. There are 75 vertical  
155 levels with 1 m resolution near the surface and 200 m in the abyss.

156 The experiments are part of the PAMIP (Polar Amplification Model Intercomparison Project)  
157 panel of CMIP6, and are described in detail in Smith et al. (2019). Three sets of simulations are  
158 performed with the coupled model using an online restoring to constrain the SIC. The specific  
159 names of these experiments are pa-pdSIC, pa-piArcSIC and pa-futArcSIC (tier 2) in Smith et al.  
160 (2019). The present-day ensemble, hereafter called PD, uses the observed SIC climatology  
161 from 1979-2008 in HadISST (Rayner et al., 2003). The pre-industrial ensemble, called PI, uses  
162 an Arctic SIC retrieved from the CMIP5 simulations, with a global mean surface temperature  
163 that is 0.57°C colder than for the reference period 1979-2008. The future ensemble, called FUT,  
164 is calculated in a similar way, but using the CMIP5 scenario simulations to produce the SIC  
165 corresponding to a global mean surface temperature 2°C warmer. The SIC field used to  
166 constrain the coupled model simulations is called the target SIC in the following. Details on the  
167 calculation of their boundary conditions are given in Smith et al. (2019). Complementary  
168 experiments to determine the uncoupled atmospheric response have also been conducted and  
169 analyzed (see discussion). The specific names of these experiments are pdSST-pdSIC, pdSST-  
170 piArcSIC and pdSST-futArcSIC (tier 1) in Smith et al. (2019). These experiments are  
171 atmosphere-only simulations, using the same SIC as the one used as the target in the coupled  
172 simulations. The simulations use a repeated climatological SST calculated from 1979-2008 in  
173 HadISST, except for the grid points where the amplitude of SIC anomalies is at least 10%  
174 compared to present-day conditions. In that case, the SST is modified using the procedures  
175 described previously for sea ice concentration.

176 All experiments used the CMIP6 external forcing corresponding to the year 2000. The  
177 experiments have a duration of 14 months (from 2000 April 1st to 2001 May 31st). Unless  
178 stated otherwise, the first two months of spin-up are excluded to avoid potential initialisation  
179 adjustments, so that time series of 12 months are finally analyzed. As previously suggested, a  
180 large number of members are needed to characterize the response to sea ice changes (Peings  
181 et al., 2021). Therefore, we performed initial-conditions ensembles of 200 members for each  
182 Arctic sea ice experiment. This makes a total of 600 14-month simulations for the coupled and  
183 also for the atmosphere-only configurations. For the coupled model simulations, the initial  
184 conditions were chosen from the available ensemble of 32 historical CMIP6 simulations with the  
185 IPSL-CM6A-LR (Bonnet et al., 2021) in the 1990-2009 period. For the atmosphere-only  
186 simulations, the initial conditions are similarly sampled from the available ensemble of AMIP  
187 runs (22 members) realized in CMIP6 with IPSL-CM6A-LR.

188 To constrain the sea ice in the coupled model simulations, we use a method analogous to a  
189 nudging of the SIC, already used in Acosta Navarro et al. (2022) with the EC-Earth model.

190 We apply a heat flux anomaly, called  $F$ , calculated as:

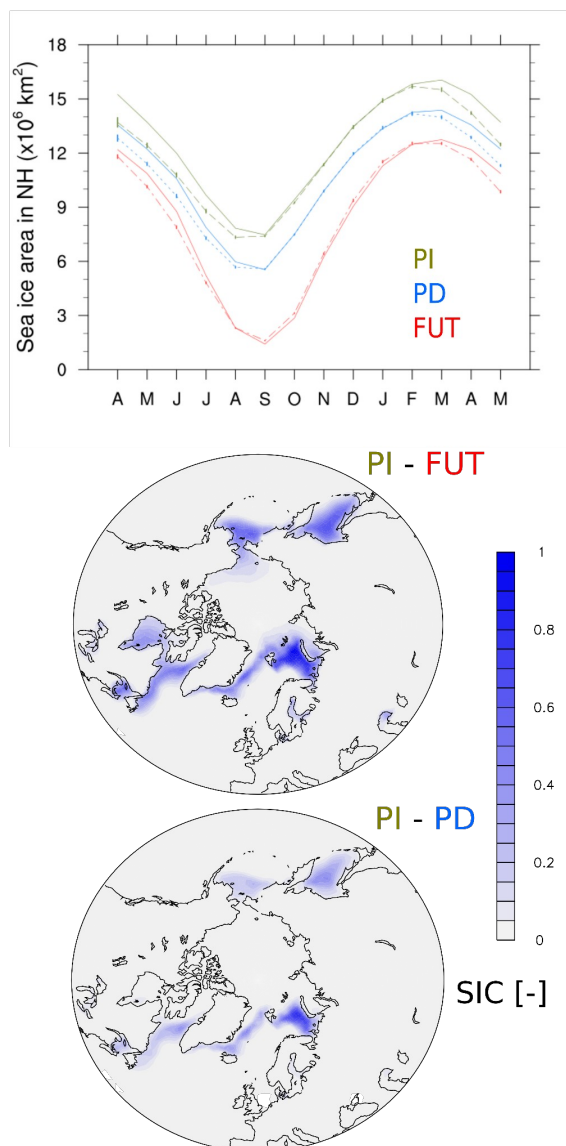
$$191 \quad F = \alpha H \Delta SIC \quad (1)$$

192 where  $H$  is the online sea ice thickness at a given grid point;  $\Delta SIC$  is the difference of actual  
193 SIC for the grid point and the target SIC; and  $\alpha$  is a relaxation coefficient. Given the short period  
194 of the simulations (14 months), we aim at reproducing the target SIC field within a few days. We



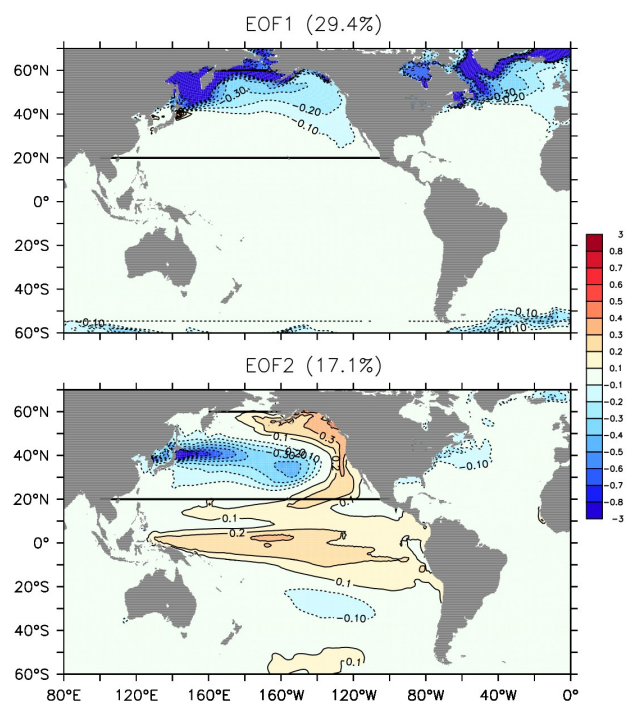
195 found that a relaxation constant of  $3500 \text{ W / m}^2 \text{ m}$  leads to little difference between the simulated  
196 and target sea ice (see Figure 1). This corresponds to a time constant of about 1 day for typical  
197 values of the latent heat of fusion and ice density. To achieve an effective nudging at short time  
198 scale, an additional flux anomaly is applied under the ice, as SST is either nudged with a  
199 relaxation coefficient of  $100 \text{ W / m}^2 \text{ K}$  (if  $\Delta SIC < 0$ ) or prescribed to the freezing point (if  $\Delta SIC >$   
200  $0$ ). The difference between two sets with different concentrations of sea ice reveals the impact  
201 of changing sea ice.

202 Figure 1 shows the Arctic SIC simulated in the coupled "pre-industrial" (PI), "present-day" (PD)  
203 and "future" (FUT) simulations. As described in Smith et al. (2019), the winter sea ice loss in  
204 FUT is mostly located in the Barents-Kara, Labrador and Chukchi Seas compared to PI. The  
205 upper panel of Fig. 1 shows the simulated ensemble mean Arctic sea ice area and compares it  
206 to the target one. From August to February, the simulated SIC of the three coupled experiments  
207 is in good agreement with the target SIC. However, they underestimate by  $\sim 0.5$  to  $1 \cdot 10^6 \text{ km}^2$  the  
208 sea ice area from April to July, with differences smaller in FUT (red lines) than in PI (green  
209 lines). The size of the confidence intervals of the ensemble mean, assuming Gaussian  
210 distribution, is small for all months, which implies that the nudging method has effectively  
211 reduced the large internal variability of the Arctic sea ice obtained in IPSL-CM6A-LR (Jiang et  
212 al., 2021).



213

214 Figure 1: (Top) Arctic sea ice area (in  $10^6 \text{ km}^2$ ) for the ensemble mean of coupled model  
215 simulations using constrained SIC for (red, dash-dotted line) FUT, (blue, dotted line) PD and  
216 (green, dash line) PI. The corresponding target sea ice is shown with solid lines. Vertical bars  
217 represent the 95% confidence interval for the ensemble mean. (Center) Simulated Arctic sea ice  
218 concentration changes in the coupled model ensembles for PI minus FUT and (Bottom) PI  
219 minus PD averaged from December to February.



220  
221

222 Figure 2: (Top) First and (bottom) second empirical orthogonal function of the yearly averaged  
223 SST between 20°N and 60°N in the Pacific ocean in the ensembles of coupled simulations.

224

225 To characterize the Pacific Ocean decadal variability, an empirical orthogonal function (EOF)  
226 analysis of the yearly sea surface temperature (SST) between 20°N and 60°N in the Pacific  
227 ocean (Fig. 2, black lines) is performed using the concatenated outputs of the ensembles PI, PD  
228 and FUT. This EOF analysis uses the member dimension instead of the time dimension, as  
229 classically used. The EOFs are defined as the regression of the SST onto the standardized  
230 principal components (PCs). The first EOF (Fig. 2 top) shows large loadings in the Chukchi,  
231 Okhotsk and Bering seas where sea ice was removed in PD and FU conditions (see Fig. 1). It is  
232 associated with anomalies of the same sign in the North Atlantic at the edges of the Arctic sea  
233 ice cover. The first PC explains 29.4% of the variability of the concatenated PI, PD and FUT  
234 members. It shows the dominant influence of the mean sea ice changes, with standardized  
235 values around 1, 0 and -1 for simulations PI, PD and FUT, respectively (not shown). The second  
236 EOF explains 17.1% of the variance and shows a horse-shoe shaped anomaly in the eastern  
237 Pacific that typically characterizes the PDO (Fig. 2, bottom). The anomalies in the eastern  
238 Pacific are associated with an equatorial Pacific SST of the same sign, reflecting the role of the  
239 El Niño Southern Oscillation (ENSO) in generating the PDO. Conversely, anomalies with the  
240 opposite sign are located in the western and central North Pacific, with maximum amplitude off  
241 Japan. This pattern is similar to the observed Pacific Decadal Oscillation in the warm phase but  
242 for the midlatitude horseshoe extending too much in the western Pacific, together with the  
243 equatorial SST anomaly, as found in many other climate models (Sheffield et al., 2013; Coburn

15

16



244 and Pryor, 2021). Hereafter, the PDO index is defined as the standardized second principal  
245 component. A positive PDO index corresponds to a warm PDO phase and a negative PDO  
246 index to a cold PDO phase.

247

248 In order to investigate the simultaneous atmospheric influence of the sea ice changes and the  
249 PDO, we use an analysis of the covariance based on a general linear model. This methodology  
250 benefits from the use of the three ensemble simulations together (600 members) and avoids  
251 building composites dependent on the arbitrary choice of a threshold. Hereafter, we only focus  
252 on the atmospheric anomalies in winter, defined as the 3-month mean in December-February-  
253 March. The atmospheric variables from the concatenated 600 members are regressed using the  
254 PDO index as a covariate and the sea ice state as a categorical independent variable with three  
255 levels. We use the PI conditions as the reference. We also consider the interactions between  
256 the sea ice and the PDO, as we find that it significantly improves the explained variance of the  
257 general linear model in many locations (not shown).

258

259 At each grid point, the general linear model is defined as follows:

260

$$\begin{aligned} 261 \quad Y(n) = & \beta_0 + \beta_{PD} [PD](n) + \beta_{FUT} [FUT](n) + \beta_{PDO} PDO(n) + \beta_{PD:PDO} [PD](n) PDO(n) \\ 262 \quad & + \beta_{FUT:PDO} [FUT](n) PDO(n) + \varepsilon \end{aligned} \quad (2)$$

263

264 where  $Y(n)$  designates the dependant variable, an atmospheric variable in simulation  $n$  ;  
265  $[PD](n)$  is a dummy variable with a value of 1 if the simulation  $n$  is from PD ensemble, and 0  
266 otherwise (same for  $[FUT](n)$  with FUT);

267  $PDO(n)$  is the PDO index for simulation  $n$  ;

268  $\beta_0$  is the intercept;

269  $\beta_{PD}$  is the regression coefficient determining the effect of the sea ice in PD (FUT) when  
270 compared to PI (same for  $\beta_{FUT}$  with FUT);

271  $\beta_{PDO}$  is the regression coefficient determining the effect of the PDO;

272  $\beta_{PD:PDO}$  is the regression coefficient determining the interaction between the PDO and the PD  
273 sea ice (same for  $\beta_{FUT:PDO}$  with FUT). It evaluates to what extent their contributions are non-  
274 additive;

275  $\varepsilon$  is a residue.

276

277 Statistical significance is estimated using a two-tailed Student's t-test for each of the regression  
278 coefficients, assuming all members independent. To account for the overestimated global  
279 significance when only using local tests, we calculate the field significance with the False  
280 discovery rate (FDR; Wilks et al., 2016) in the Northern Hemisphere between 20°N and 80°N.  
281 We choose a FDR p-value of  $\alpha_{FDR} = 20\%$  to achieve a global test level at 10%, assuming a  
282 spatial decorrelation of  $\sim 1.54 \cdot 10^3$  km, which is consistent with the previous estimations using the  
283 500-hPa geopotential height (Polyak, 1996).



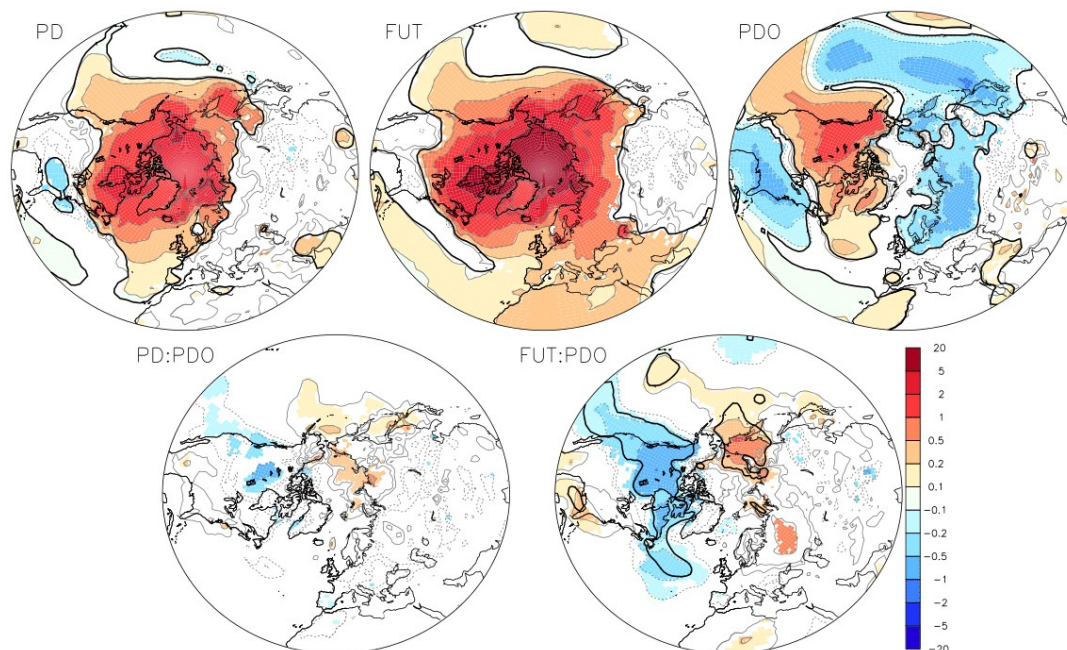
## Results

284

285

286 We first analyze the effect of the sea ice loss in winter by comparing PD with PI (PD-PI) and  
287 FUT with PI (FUT-PI) in the coupled simulations, using the general linear model. We then  
288 investigate the impacts of the PDO and finally how they are modulated by the sea ice loss,  
289 using a warm (i.e. positive) PDO phase for illustration.

290 The air temperature at 2m (Fig. 3) shows as expected a significant warming over the polar cap  
291 of about 4°C when comparing PD and PI (top-left) and about 10°C when comparing FUT and PI  
292 (top-middle). In its warm phase, the PDO induces warming over the northwest America of about  
293 2°C and a cooling over the North Pacific, over Siberia and south of the North America continent  
294 of about 1°C (top-right). The interaction term between the sea ice loss and the PDO is non-  
295 negligible (bottom), showing a cooling over North America and warming over northeast Siberia,  
296 which thus contributes to slight regional damping of the PDO teleconnections. However, this  
297 interaction term is larger for FUT than for PD, and is barely significant for PD sea ice loss. A  
298 warm PDO thus modulates the sea ice impact by minimizing the warming in North America and  
299 enhancing the warming in northeast Asia. As the analysis is linear, a cold PDO phase will lead  
300 to the opposite effect to a warm PDO phase, but the interaction between sea ice loss and the  
301 cold PDO still results in a damping of the PDO teleconnections.



302

303 Figure 3: Surface air temperature at 2m (in °C) in response to the sea ice loss and PDO in the  
304 coupled simulations when using an analysis of the covariance: (top-left panel) effect of the PD

19

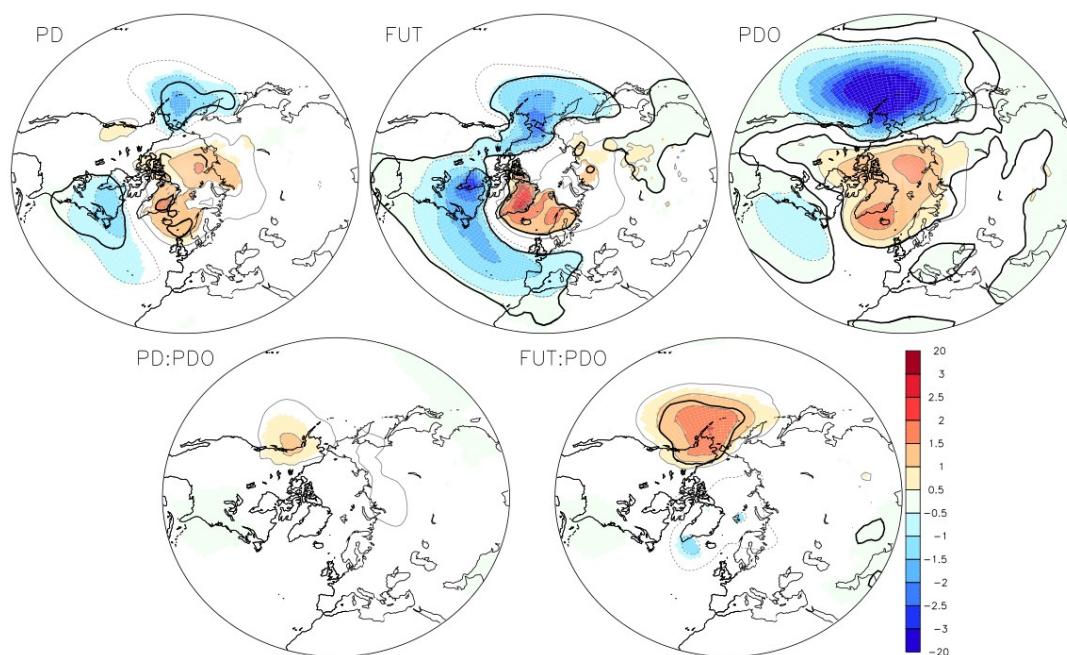
20

10



305 sea ice loss ( $\beta_{PD}$  in Eq. (2)); (top-middle) effect of the FU sea ice loss ( $\beta_{FUT}$  in Eq. (2)) (top-right)  
306 effect of a warm PDO ( $\beta_{PDO}$  in Eq. (2)); (bottom-left) effect of the interaction between PD sea ice  
307 loss and the PDO ( $\beta_{PD:PDO}$  in Eq. (2), and (bottom-right) effect of the interaction between the  
308 FUT sea ice loss and the PDO ( $\beta_{FUT:PDO}$  in Eq. (2)). The color shades a p-value below 10%.  
309 The black line indicates field significance, as given by the false discovery rate.

310 The Arctic sea ice loss additionally induces a significant deepening of the Aleutian Low and a  
311 negative NAO-like response. This is shown by the negative sea level pressure anomalies over  
312 the Northern Pacific and central Atlantic, together with positive sea level pressure anomalies  
313 from Greenland to Norway (Fig. 4, top-left and top-center), with larger and broader anomalies in  
314 FUT than in PD. The geopotential height at 500-hPa (Fig. 5, top-left and top-center) also shows  
315 a strong increase over the polar cap in response to sea ice loss. It increases above Greenland  
316 by as much as 20 m in PD, and 40 m in FUT, which is consistent with the surface warming and  
317 the associated increase of the lower tropospheric thickness. A negative AO pattern is also  
318 found: the geopotential height at 500-hPa decreases by approximately 15 m over a band from  
319 western North America to the Iberian Peninsula. Melting Arctic sea ice also induces a small but  
320 significant deepening of the Aleutian low at 500 hPa. In the stratosphere, the geopotential at 50-  
321 hPa increases over the polar cap in both FUT and PD cases and slightly decreases over  
322 southern Europe for PD and over northern Europe for FUT (Fig. 6, top-left and top-right). Figure  
323 7 (top-left and top-right) further shows the zonal mean zonal wind changes, with a significant  
324 weakening of the poleward flank of the eddy-driven jet and of the polar vortex between 50°N  
325 and 70°N due to sea ice loss. Between 30°N and 40°N the zonal wind is intensified from the  
326 surface to 70 hPa, at the core of the subtropical jet. The zonal wind also decreases south of  
327 20°N, in line with a shrinking of the subtropical jet.  
328



329

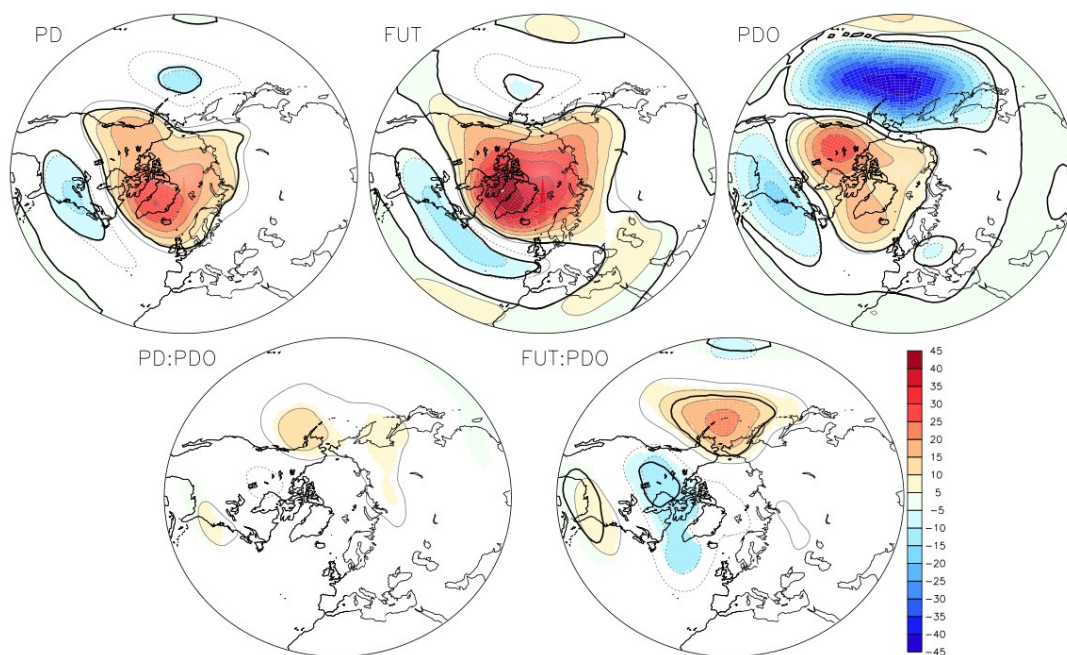
330 Fig 4: Same as Fig. 3 but for sea level pressure, in hPa.

331 The experiments can also be used to investigate the influence of a positive PDO on the  
332 atmosphere. A warm PDO induces a significant positive Pacific-North American-like (PNA)  
333 pattern, with a strong strengthening of the Aleutian Low, a ridge over Northwest America/polar  
334 cap, and a small geopotential height increase over southeastern North America (Figs. 4 and 5,  
335 top-right). Such impacts are consistent with the influence of the warm equatorial Pacific SST  
336 anomalies associated with the PDO onto the PNA (Trenberth and Hurrell, 1994; Newman et al.,  
337 2016). In the stratosphere, the geopotential height at 50-hPa shows a tripole pattern with a high  
338 over the Arctic and two lows over the eastern North Pacific and Europe, resembling the negative  
339 phase of the Arctic Oscillation (Fig. 6, top-right). The warm PDO induces a significant  
340 weakening of the poleward flank of the eddy-driven jet from 50°N to 70°N, as well as a  
341 weakening of the stratospheric polar vortex between 50°N and 80°N (Fig. 7, top-right). The  
342 zonal winds also show a large increase between 20°N and 40°N at the core of the subtropical  
343 jet. Such PDO impacts are consistent with findings linking the PDO to the stratosphere based  
344 on observations (Woo et al., 2015) and models (Hurwitz et al. 2012; Kren et al. 2016).  
345 Nevertheless, it remains unclear whether the stratospheric impacts of the PDO are linked to the  
346 extratropical part of the PDO pattern or to the associated equatorial SST anomalies. Indeed,  
347 warm equatorial SST anomalies associated with an El Niño have been previously shown to  
348 drive a weakening of the Aleutian low, which leads to decreased momentum flux from upward  
349 propagating planetary waves that weaken the stratospheric polar vortex (Manzini et al., 2006;  
350 Hurwitz et al., 2012; Woo et al., 2015; Kren et al., 2016; Domeisen et al., 2019), a response that  
351 is consistent with our regression result for the PDO.

23

24

12

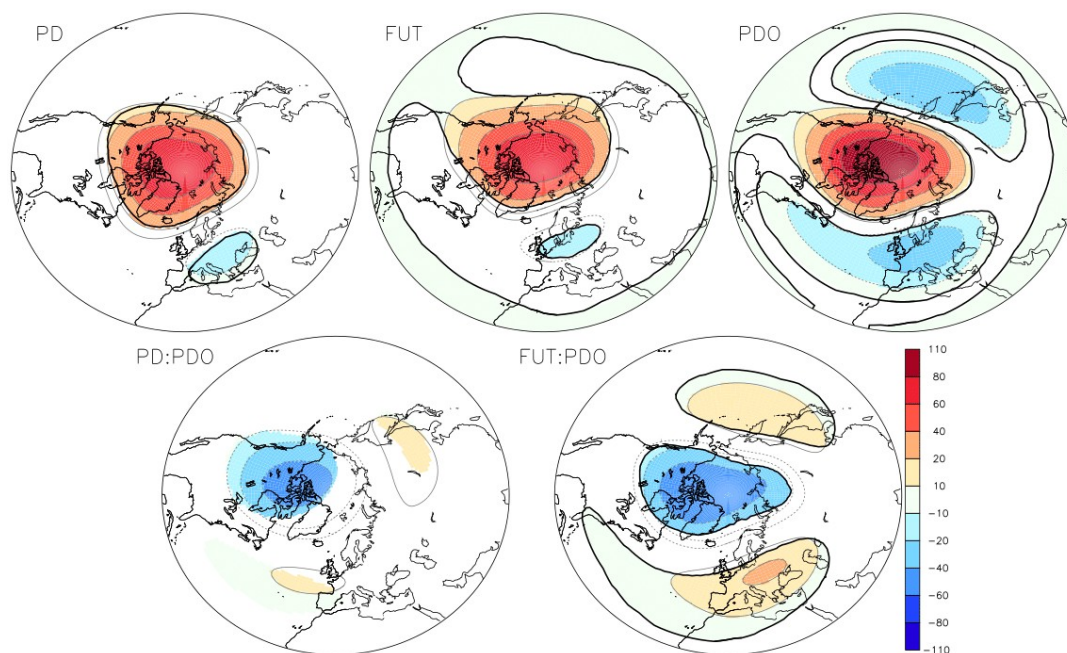


352

353 Figure 5: Same as Figure 3 but for geopotential height at 500 hPa, in m.



354

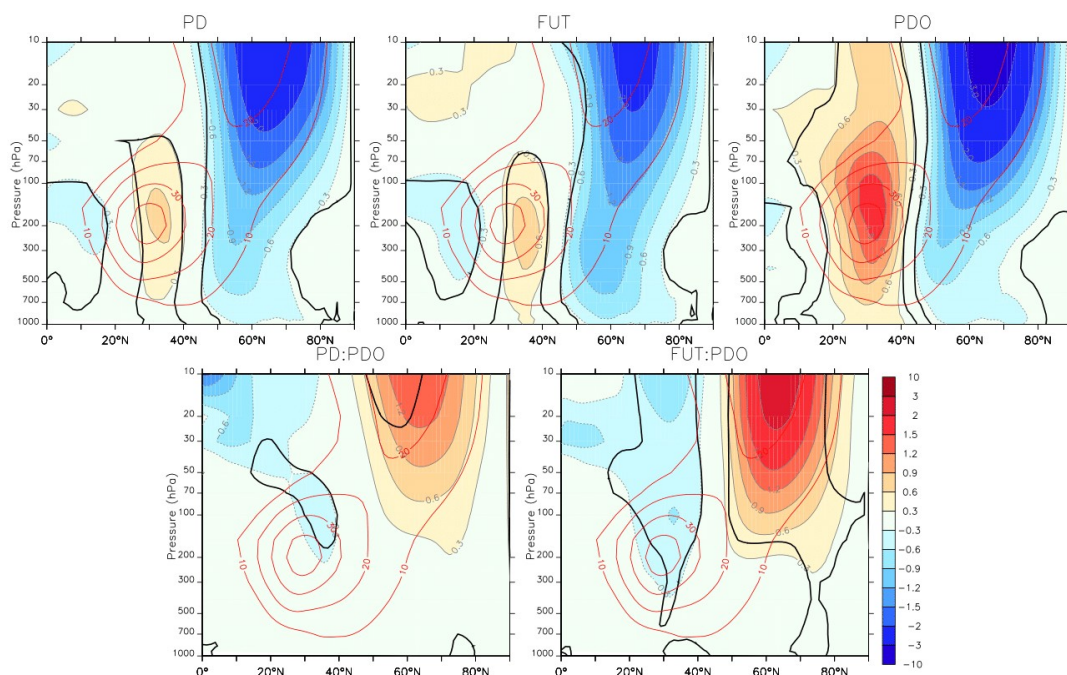


355

356 Figure 6: Same as Figure 3 but for geopotential height at 50 hPa, in m.

357 The interaction between sea ice loss and the PDO leads to a weakening of the Aleutian Low  
358 (Fig. 4, bottom) and a pattern reminiscent of a wave train at 500 hPa, resembling a negative  
359 PNA phase (Fig. 5, bottom). The results of the interaction between sea ice loss and PDO are  
360 qualitatively robust regardless of the magnitude of the sea ice loss (e.g. FUT or PD), but the  
361 amplitude of the interaction is small and it is only significant in FUT. In PD, the interaction shows  
362 local p-values below 10% but is not field significant. Also, the effect of interaction is stronger and  
363 more significant in the stratosphere. At 50 hPa, a significant strengthening of the polar vortex is  
364 found, with negative anomalies above the polar cap and positive anomalies over the northwest  
365 Pacific and Europe (Fig. 6, bottom). Again, the stratospheric polar vortex increase is stronger  
366 and more significant for FUT than for PD. The interaction between PDO and sea ice loss also  
367 shows zonal wind changes consistent with a strengthening of the polar vortex (Fig. 7, bottom).  
368 Hence, the PDO teleconnections in both troposphere and stratosphere are damped under sea  
369 ice loss conditions, in particular for the stratosphere.

370



371

372 Figure 7: Same as Figure 3 but for zonal mean zonal winds, in  $\text{m s}^{-1}$ . The black line indicates a  
373 p-value below 10%.

374 To understand the causes of the zonal mean wind changes, the zonal-mean diagnostics of  
375 transformed eulerian mean quantities are derived following Andrews et al. (1987). In response  
376 to FUT sea ice melting, the warming located north of  $40^\circ\text{N}$  is amplified toward the surface in the  
377 lower troposphere but extends throughout the troposphere (Fig. 8, top-left). There is also an  
378 important warming in the stratosphere from 100 hPa to 10 hPa over the polar cap, north of  
379  $60^\circ\text{N}$ . The troposphere also warms between  $20^\circ\text{N}$  and  $30^\circ\text{N}$ , which can be linked to the  
380 shrinking of the subtropical jet (see Fig. 7). A warm PDO phase also leads to a stratospheric  
381 warming (Fig. 8, top-right) and a polar vortex weakening (Fig. 7, top-right). However, it is  
382 associated with a warming of the tropical troposphere that is intensified in the upper  
383 troposphere. The warming over the Arctic associated with a positive PDO is rather uniform and  
384 is not intensified at the surface. A quasi-barotropic cooling is also located at  $40^\circ\text{N}$ .

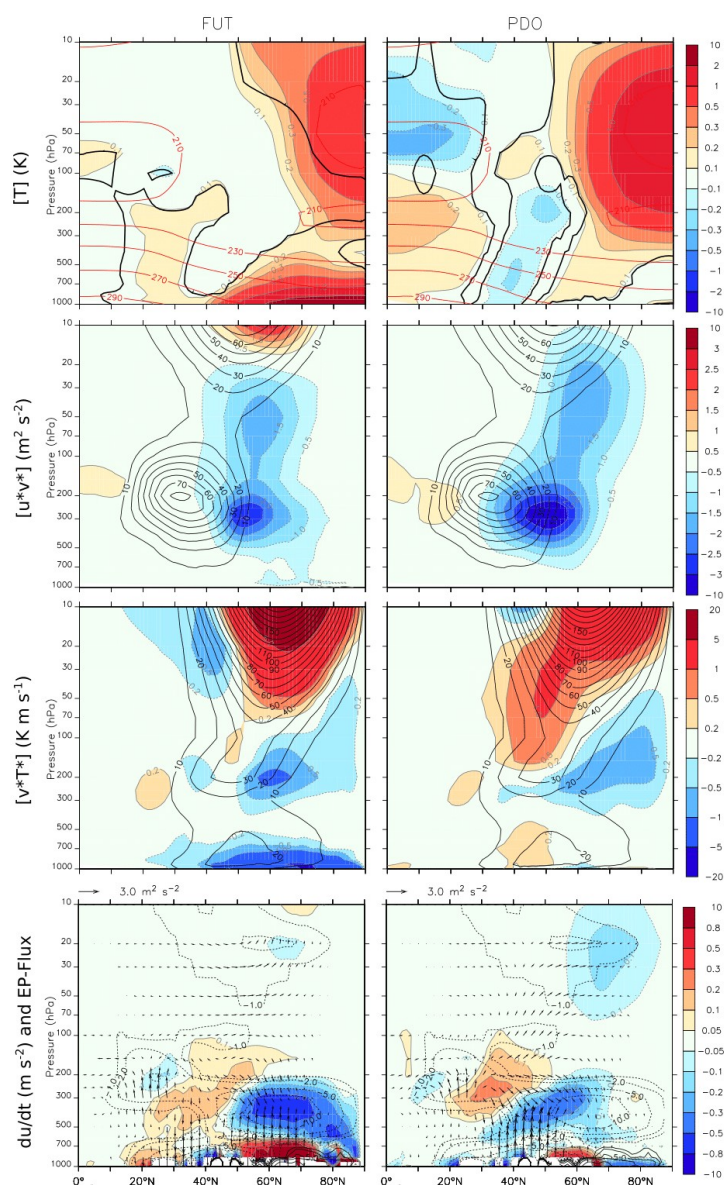
385 Both sea ice loss and PDO lead to a reduced eddy momentum flux at the poleward flank of the  
386 subtropical jet peaking around 300 hPa and extending into the stratosphere (Fig. 8, second  
387 row). The eddy heat flux (third row) weakens at the lower-troposphere in response to sea ice  
388 loss. In addition, both sea ice loss and warm PDO decrease the eddy heat flux between  $50^\circ\text{N}$   
389 and  $80^\circ\text{N}$  in the lower-stratosphere at 200-hPa, while increasing it above 100-hPa. The  
390 anomalous Eliassen–Palm (EP) flux is shown in Fig. 8, (bottom row; vectors), as well as the  
391 zonal wind acceleration implied by the EP flux divergence (bottom row; shading). In normal  
392 conditions, the EP flux is directed upward and equatorward (not shown) and it converges into  
393 the upper troposphere, with two local maximums (Fig. 8, bottom row; contours). One maximum

29

30



394 is located at 25°N 200-hPa, while the other maximum is between 55°N and 75°N at 400-hPa.  
395 This convergence acts to decelerate the zonal wind. The FUT sea ice loss reinforces the  
396 convergence between 55°N and 75°N at 400-hPa, with an anomalous upward EP flux in the  
397 lower troposphere below (Fig. 8, bottom; color shade). We verified that the convergence is due  
398 to the vertical component of the EP flux which is proportional to the ratio between the eddy heat  
399 flux and the stratification. As the meridional eddy heat flux shows negative anomalies in this  
400 region, the intensification of the upward heat flux in 55°N-75°N mainly results from the weaker  
401 atmospheric stratification, leading to a more unstable atmosphere. Between 30°N and 40°N, the  
402 EP flux is instead oriented downward in the troposphere, which leads to anomalous divergence  
403 between 500-hPa and 200-hPa. It corresponds to the intensification of the core of the  
404 subtropical jet in Fig. 7 (top-center). This change is again dominated by the vertical component  
405 of the EP flux (not shown) and might reflect the weakening of the meridional eddy heat flux. The  
406 same analysis for the PDO influence shows EP flux anomalies somehow similar to those  
407 associated with sea ice loss. However, the intensification of the EP flux convergence is located  
408 between 40°N and 60°, and the EP flux upper-tropospheric divergence at 30°N is more intense.  
409 These changes are again associated with the vertical component of the EP flux (not shown)  
410 associated with an intensification of the tropospheric meridional eddy heat flux between 30°N  
411 and 40°N. In both sea ice loss and PDO cases; the changes of the eddy momentum flux can be  
412 described as a positive feedback reinforcing the changes of the eddy heat flux, as in Smith et al.  
413 (2022). In the stratosphere, a clear intensification of the EP flux is simulated poleward and  
414 upward in response to sea ice loss and PDO, consistent with the weakening of the polar vortex.



415

416 Figure 8: Zonal mean temperature and atmospheric circulation changes related to (left panels)  
 417 sea ice loss in FUT and (right panels) PDO. Temperature (in K; 1st row), eddy momentum flux  
 418 ( $u^*v^*$  in  $m^2 \cdot s^{-2}$ ; 2nd row), eddy heat flux ( $v^*T^*$  in  $K \cdot m \cdot s^{-1}$ ; 3rd row), zonal wind tendency implied  
 419 by the Eliassen-Palm flux divergence (in  $10^2 m \cdot s^{-1} \cdot day^{-1}$ ; bottom row, color shade) and  
 420 Eliassen-Palm flux ( $m^2 \cdot s^{-2}$ ; bottom row, vectors). In the bottom row, the black contours show the  
 421 zonal wind tendency implied by the Eliassen-Palm flux divergence in the PI ensemble, chosen  
 422 as a reference. The regressions with a p-value below 10% are indicated by a thick black line in  
 423 the top panel.

33

34

17



## SUMMARY & DISCUSSION

424

425

426 We performed sensitivity experiments with the IPSL-CM6A climate model to study the short  
427 term response (within 14 months) to the Arctic sea ice loss. We focussed on the winter (DJF)  
428 atmospheric circulation changes and how the PDO interacts with the sea ice impacts. The  
429 simulations show a robust negative NAO-like pattern in response to sea ice melting, in line with  
430 most studies (Deser et al., 2015; Screen et al., 2018; Simon et al., 2021). A positive PNA with a  
431 strong deepening of the Aleutian Low is simulated in response to warm PDO, which is a well-  
432 established teleconnection (Trenberth et al., 1998; Mantua et al., 2002; Li et al., 2007). The  
433 response to Arctic sea ice loss also includes a small deepening of the Aleutian low, as in  
434 Blackport and Screen (2019). The discrepancy with other studies in sign (Cjivanovic et al., 2017;  
435 Simon et al., 2021) or in amplitude (Screen et al., 2018) can be explained by the timescale  
436 investigated. Both Blackport and Screen (2019) and our study are focused on short response  
437 time scales less than 5 years, which might be too short to affect the trade winds and to generate  
438 SST anomalies in the tropics. The sea ice melting and the PDO were found to generate similar  
439 atmospheric circulation changes. Both lead to a weakening of the eddy-driven jet on its  
440 poleward flank, an intensification of the subtropical jet and a weakening of the polar vortex.  
441 However, for the sea ice loss, these changes are governed by the lower-tropospheric warming  
442 north of 50°N and the weaker lower-tropospheric meridional temperature gradient. The  
443 weakening of the eddy-driven jet on its poleward flank is induced by weaker surface  
444 stratification leading to increased upward Eliassen-Palm flux and acting to reduce the mean  
445 zonal flow. Conversely, a warm PDO phase mainly intensifies the transient eddy heat flux at  
446 30°N-40°N, probably through the intensification of the stationary wave pattern. The combined  
447 response of the mid-latitude atmospheric circulation to a warm PDO and sea ice melting is not  
448 additive, with the interaction between both signals being partly destructive. When sea ice melts  
449 during a warm PDO phase, the impacts are smaller than the ones expected by the addition of  
450 the two effects. This applies to the anomalies simulated in both the troposphere and  
451 stratosphere.

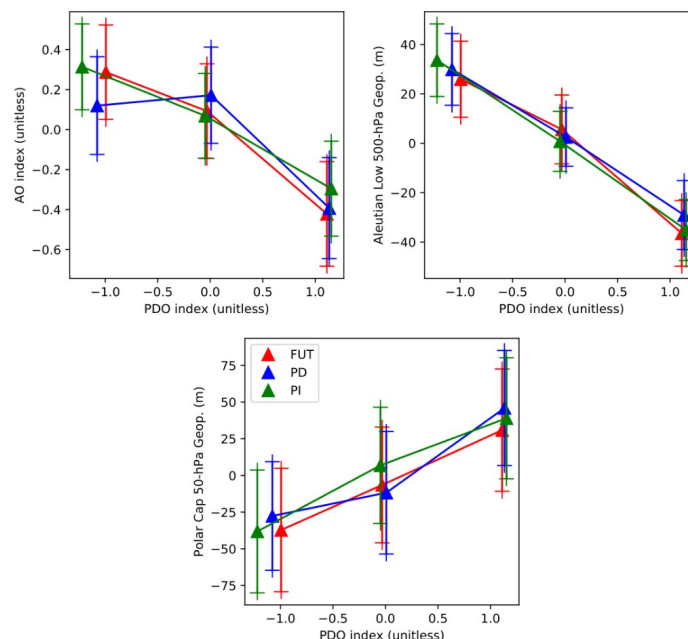
452

453 The general linear model presented here can be applied to the analysis of other modes of  
454 climate variability or ensembles of sensitivity experiments, such as the idealized experiments of  
455 the DCPP panel of CMIP6. The model uses all the ensemble members when estimating the  
456 different influences, which are thus based on a larger sample than in traditional methods, and it  
457 does not involve the choice of an arbitrary threshold, as when building composites. However,  
458 the method does not account for non-linearities, and the impacts of warm and cold PDO could  
459 be asymmetric. However, we verified that the changes of the Aleutian low and the polar vortex  
460 are symmetric in composites based on the PDO index (Figure 9; top). The AO pattern is only  
461 slightly asymmetric in the present-day sea ice conditions, when the neutral and cold PDO states  
462 have a similar AO impact (Fig. 9). The AO pattern is symmetric in the preindustrial and future  
463 sea ice conditions. Hence, the linear analysis seems applicable to a good approximation.

464

35

36



465

466

467 Figure 9: Mean AO index (top-left; unitless), Aleutian low (top-right; in m) and polar cap 50 hPa  
 468 geopotential height (bottom, in m), for members sorted following the PDO index for the PI  
 469 (green lines), PD (blue lines) and FUT (red lines) ensembles. The triangles indicate the value for  
 470  $PDO < Q_{1/3}$ ,  $Q_{1/3} < PDO < Q_{2/3}$  and  $PDO > Q_{2/3}$ , where  $Q_{1/3}$  and  $Q_{2/3}$  indicate the first and second  
 471 tercile of a gaussian distribution. The error bar provides the 95% confidence interval. The AO  
 472 index is calculated as the first principal component of the 500-hPa geopotential height using all  
 473 the members. The Aleutian low index is the anomaly of the 500-hPa geopotential height in  
 474  $150^{\circ}\text{E}-180^{\circ}\text{E } 40^{\circ}\text{N}-50^{\circ}\text{N}$ . The polar cap 50-hPa anomalies is calculated with the mean value of  
 475 the 50-hPa geopotential north of  $60^{\circ}\text{N}$ .

476

477 Concerning the amplitude of the response to sea ice loss, observational study estimates that  
 478 winter Arctic sea ice loss could have led to a much larger increase, perhaps as much as 200 m  
 479 over Iceland at 500 hPa over the last four decades if linearity and perpetual winter conditions  
 480 could be assumed, although it should be less in more realistic conditions (Simon et al., 2020).  
 481 Nonetheless, the Arctic sea ice loss impact on the NAO is smaller in our sensitivity experiments  
 482 (30 to 50 m). The reasons for this discrepancy are under active debate (Cohen et al., 2020). This  
 483 might be explained by too weak eddy feedback represented in models (Smith et al., 2022) but  
 484 also by the difficulty to cleanly attribute a response to Arctic sea ice decline in observations.  
 485 Here, we show that the PDO is an important confounding factor that has an impact on the Arctic  
 486 similar to that of Arctic sea ice loss, especially in the stratosphere. Much care is therefore  
 487 needed to separate these two effects when using observations. Moreover, depending on the  
 488 protocol used to constrain the sea ice in coupled model sensitivity experiments, the amplitude of  
 489 the atmospheric response to sea ice loss can vary by a factor of two (Simon et al, 2021). The

37

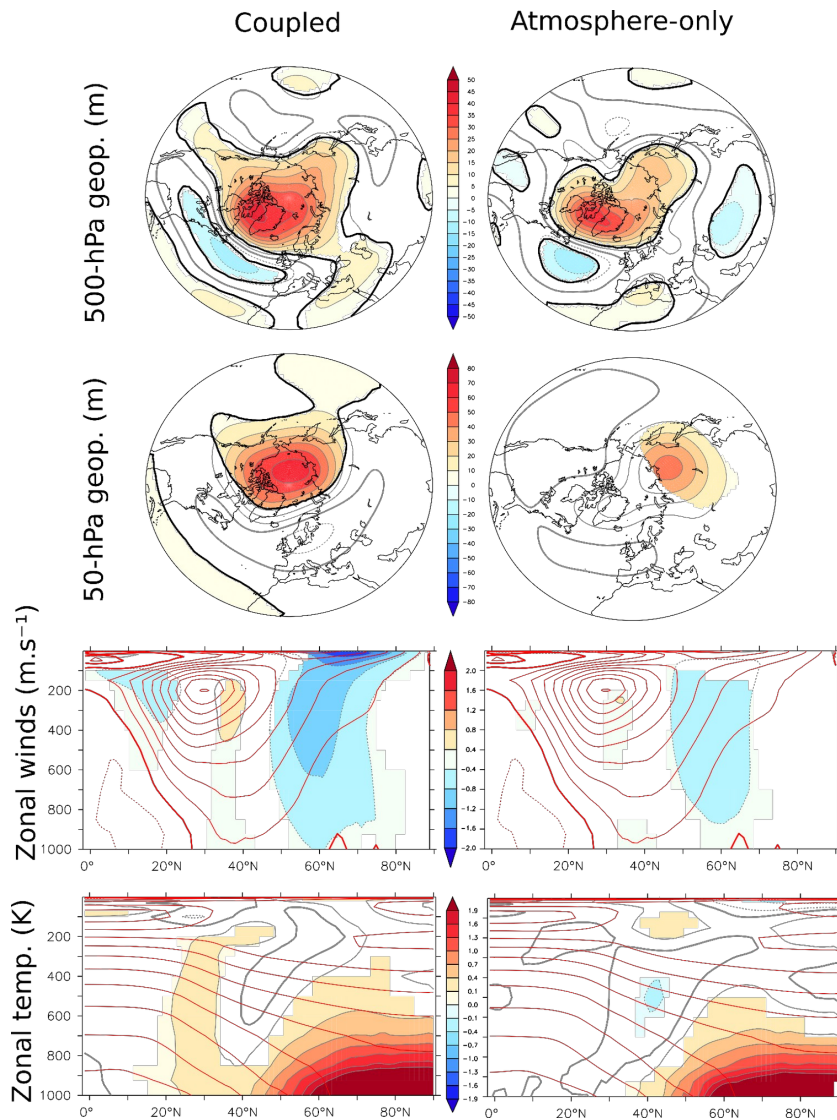


490 simulated changes might therefore depend on the methodology used to constrain the sea ice  
491 cover. Moreover, the sea ice thickness was not constrained in the sensitivity experiments but  
492 might play an important role in the atmospheric circulation response (Lang et al., 2017).

493

494 The bulk of our analysis was based on simulations with an ocean-atmosphere general  
495 circulation model. However, a different response to sea ice loss might be obtained with  
496 atmospheric-only configurations where the two-way air-sea coupling is not allowed. Studies  
497 have primarily investigated the ocean feedback on timescales from decadal to centennial. Deser  
498 et al. (2015) found that full ocean coupling amplifies the Arctic sea ice loss impact in 100-year  
499 simulations, while no feedback was found in an atmospheric model coupled to a slab ocean at  
500 decadal timescale in Cvijanovic et al. (2017). However, few studies have investigated short  
501 simulations of 14 months, where only fast feedbacks can operate. To determine the role of the  
502 coupling, we have performed the same sensitivity experiments but using the atmosphere-only  
503 configuration of the IPSL-CM6A model (hereafter ATM). We show that the tropospheric  
504 circulation response to sea ice loss is very similar to that in the coupled experiments, although  
505 the increase of the 500-hPa geopotential height over the Arctic is weaker in the ATM model (Fig  
506 10, top). Besides, the coupled simulations present a stronger weakening of the stratospheric  
507 polar vortex than the atmospheric-only simulations (Fig. 10, middle rows). The lower  
508 troposphere warming is more intense in the coupled model, which reflects the presence of sea  
509 ice-atmosphere feedbacks, such as those involving thinner sea ice. This leads to a more intense  
510 decrease of the tropospheric stratification and intensifies the upward planetary wave  
511 propagation into the stratosphere. Since the tropospheric response to a weakened polar vortex  
512 resembles the negative AO (Baldwin and Dunkerton, 1999; Kidston, 2015, Cohen et al, 2017;  
513 Hoshi et al. 2019), the stronger stratospheric polar vortex weakening might explain the larger  
514 AO anomaly in the coupled experiments.

515



516  
 517 Figure 10: Difference between 200-members ensemble of FU and PI (color and gray outline) in  
 518 DJF for the geopotential height at 500-hPa (m; top), the geopotential height at 50-hPa (m;  
 519 middle-top), the zonally averaged zonal wind (m/s; middle-bottom) and the zonally averaged  
 520 temperature (K; bottom) in the coupled (left) and atmosphere-only (right) configurations of the  
 521 IPSL-CM6A-LR. Colors are masked if the confidence level of the Student's t-test is less than  
 522 90%. The 90% confidence level based on the False Discovery Rate (FDR) is given in black  
 523 contours for the two top rows. On the middle-bottom and bottom panels, the zonal mean of the  
 524 wind zonal of the PI simulation in DJF is indicated by the red contours with an interval of 5 m s<sup>-1</sup>,  
 525 the thick red line indicates zero, solid line positive values and dashed line negative values.

526

41

42



527 We applied the same analysis as for the PDO to investigate the AMV, defined as the SST over  
528 0°N°60N-0°W80W, influence and its modulation by sea ice loss in the sensitivity experiments  
529 with the coupled model, similarly using its distribution among members resulting from the  
530 different initial North Atlantic conditions. It was further applied to the quasi-biennial oscillation  
531 (QBO) defined as the equatorial zonal wind at 30-hPa. In both QBO and AMV cases, their  
532 identified impacts onto the atmospheric circulation were barely significant, and there was no  
533 significant interaction with sea ice loss (not shown).

534 The ocean changes were not investigated in these short simulations, as they are likely to be  
535 small and confined to the surface mixed layer. However, the sea ice loss impacts onto the  
536 ocean could be very different in longer simulations. Indeed, the atmospheric response to sea  
537 ice loss can be different in transient (a few decades) or equilibrium conditions (more than five  
538 decades) (Simon et al., 2021; Blackport and Kushner, 2016; Liu and Fedorov, 2019). In  
539 particular, the changes in the Beaufort Gyre (Lique et al., 2018), the North Atlantic inflow (Simon  
540 et al., 2021) and the Atlantic Meridional Oceanic circulation (Sévellec et al. 2017) would play an  
541 important role.

542  
543  
544  
545  
546  
547  
548  
549  
550  
551  
552  
553  
554  
555  
556  
557  
558  
559  
560  
561  
562  
563  
564  
565  
566  
567



## 568 **Acknowledgements**

569 This research was supported by the Blue-Action project (European Union's Horizon  
570 2020 Research and Innovation Programme, Grant 727852).

## 571 **Code and data availability**

572 Supporting information that may be useful in reproducing the authors' work is available  
573 from the authors upon request ([ajsimon@fc.ul.pt](mailto:ajsimon@fc.ul.pt) or  
574 [guillaume.gastineau@locean.ipsl.fr](mailto:guillaume.gastineau@locean.ipsl.fr)).

575

## 576 **Author contributions**

577 AS, GG and CF contributed to the conceptualization of the study and the scientific  
578 interpretation of the results. VL and PO developed and coded the nudging method. AS  
579 and GG performed the simulations and analysis. GG carried out the Eliassen-Palm flux  
580 calculation. AS prepared the first version of the manuscript and, GG, CF and PO have  
581 reviewed and edited the manuscript.

## 582 **Competing interests**

583 The authors declare that they have no known competing financial interests or personal  
584 relationships that could have appeared to influence the work reported in this manuscript.

585

586

587

588

589

590

591

592

593

594

595

596

597

598

599

600

601

602

45

46



## REFERENCES

603

604

605 Acosta Navarro J.C., García-Serrano J., Lapin V. and Ortega P. "Added value of assimilating  
606 springtime Arctic sea ice concentration in summer-fall climate predictions", Environmental  
607 Research Letters, Under review

608

609 Andrews, D. G., Leovy, C. B., & Holton, J. R. (1987). Middle atmosphere dynamics (Vol. 40).  
610 New York: Academic Press.

611

612 Aumont, O., Éthé, C., Tagliabue, A., Bopp, L., & Gehlen, M. (2015). PISCES-v2: an ocean  
613 biogeochemical model for carbon and ecosystem studies. *Geoscientific Model Development*,  
614 8(8), 2465-2513.

615

616 Baldwin, M. P., & Dunkerton, T. J. (1999). Propagation of the Arctic Oscillation from the  
617 stratosphere to the troposphere. *Journal of Geophysical Research: Atmospheres*, 104(D24),  
618 30937-30946.

619

620 Blackport, R., & Kushner, P. J. (2016). The transient and equilibrium climate response to rapid  
621 summertime sea-ice loss in CCSM4. *Journal of Climate*, 29(2), 401-417.

622

623 Blackport, R., & Screen, J. A. (2019). Influence of Arctic sea ice loss in autumn compared to  
624 that in winter on the atmospheric circulation. *Geophysical Research Letters*, 46(4), 2213-2221.

625

626 Blackport, R., & Screen, J. A. (2020). Weakened evidence for mid-latitude impacts of Arctic  
627 warming. *Nature Climate Change*, 10(12), 1065-1066.

628

629 Boucher, O., Servonnat, J., Albright, A. L., Aumont, O., Balkanski, Y., Bastrikov, V., ... &  
630 Vuichard, N. (2020). Presentation and evaluation of the IPSL-CM6A-LR climate model. *Journal*  
631 *of Advances in Modeling Earth Systems*, 12(7), e2019MS002010.

632

633 Cassano, E. N., Cassano, J. J., Higgins, M. E., & Serreze, M. C. (2014). Atmospheric impacts of  
634 an Arctic sea ice minimum as seen in the Community Atmosphere Model. *International Journal*  
635 *of Climatology*, 34(3), 766-779.

636

637 Cheruy, F., Ducharne, A., Hourdin, F., Musat, I., Vignon, É., Gastineau, G., ... & Zhao, Y.  
638 (2020). Improved near-surface continental climate in IPSL-CM6A-LR by combined evolutions of  
639 atmospheric and land surface physics. *Journal of Advances in Modeling Earth Systems*, 12(10),  
640 e2019MS002005.

641

642 Coburn, J., & Pryor, S. C. (2021). Differential Credibility of Climate Modes in CMIP6, *Journal of*  
643 *Climate*, 34(20), 8145-8164.

644

47

48



- 645 Cohen, J., Screen, J. A., Furtado, J. C., Barlow, M., Whittleston, D., Coumou, D., ... & Jones, J.  
646 (2014). Recent Arctic amplification and extreme mid-latitude weather. *Nature geoscience*, 7(9),  
647 627  
648
- 649 Cohen, J., Zhang, X., Francis, J., Jung, T., Kwok, R., Overland, J., Ballinger, T. J., Bhatt, U. S.,  
650 Chen, H. W., Coumou, D., Feldstein, S., Gu, H., Handorf, D., Henderson, G., Ionita, M.,  
651 Kretschmer, M., Laliberte, F., Lee, S., Linderholm, H. W., ... Yoon, J. (2020). Divergent  
652 consensus on Arctic amplification influence on midlatitude severe winter weather. *Nature*  
653 *Climate Change*, 10(1), 20-29. <https://doi.org/10.1038/s41558-019-0662-y>  
654
- 655 Coumou, D., Di Capua, G., Vavrus, S., Wang, L., & Wang, S. (2018). The influence of Arctic  
656 amplification on mid-latitude summer circulation. *Nature Communications*, 9(1), 1-12.  
657
- 658 Cvijanovic, I., Santer, B. D., Bonfils, C., Lucas, D. D., Chiang, J. C., & Zimmerman, S. (2017).  
659 Future loss of Arctic sea-ice cover could drive a substantial decrease in California's rainfall.  
660 *Nature communications*, 8(1), 1-10.  
661
- 662 Czaja, A., and C. Frankignoul, (1999): Influence of the North Atlantic SST on the atmospheric  
663 circulation. *Geophys. Res. Lett.*, 26, 2969–2972, <https://doi.org/10.1029/1999GL900613>.  
664
- 665 Czaja, A., & Frankignoul, C. (2002). Observed impact of Atlantic SST anomalies on the North  
666 Atlantic Oscillation. *Journal of Climate*, 15(6), 606-623.  
667
- 668 Dai, A., & Song, M. (2020). Little influence of Arctic amplification on mid-latitude climate. *Nature*  
669 *Climate Change*. doi:10.1038/s41558-020-0694-3  
670
- 671 Deser, C., Tomas, R. A., & Sun, L. (2015). The role of ocean–atmosphere coupling in the zonal-  
672 mean atmospheric response to Arctic sea-ice loss. *Journal of Climate*, 28(6), 2168-2186.  
673
- 674 Domeisen, D. I., Garfinkel, C. I., & Butler, A. H. (2019). The teleconnection of El Niño Southern  
675 Oscillation to the stratosphere. *Reviews of Geophysics*, 57(1), 5-47  
676
- 677 Eyring, V., Bony, S., Meehl, G. A., Senior, C. A., Stevens, B., Stouffer, R. J., & Taylor, K. E.  
678 (2016). Overview of the Coupled Model Intercomparison Project Phase 6 (CMIP6) experimental  
679 design and organization. *Geoscientific Model Development*, 9(5), 1937-1958.  
680
- 681 Garcia-Serrano, J., C. Frankignoul, G. Gastineau, and A. de la Camara, 2015: On the  
682 predictability of the winter Euro-Atlantic climate: lagged influence of autumn Arctic sea ice. *J.*  
683 *Climate*, 28, 5195-5216 , [doi.org/10.1175/JCLI-D-14-00472.1](https://doi.org/10.1175/JCLI-D-14-00472.1)  
684
- 685 Garfinkel, C. I., Hartmann, D. L., & Sassi, F. (2010). Tropospheric precursors of anomalous  
686 Northern Hemisphere stratospheric polar vortices. *Journal of Climate*, 23(12), 3282-3299.  
687



- 688 Gastineau, G., J. Garcia-Serrano, and C. Frankignoul, 2017: The influence of autumnal  
689 Eurasian snow cover on climate and its links with Arctic sea ice cover. *J. Climate*, 30, 7599-  
690 7619 doi.org/10.1175/JCLI-D-16-0623.1  
691  
692  
693  
694 Hourdin, Frédéric, et al. "LMDZ6A: The atmospheric component of the IPSL climate model with  
695 improved and better tuned physics." *Journal of Advances in Modeling Earth Systems* 12.7  
696 (2020): e2019MS001892.  
697  
698 Hoshi, K., Ukita, J., Honda, M., Nakamura, T., Yamazaki, K., Miyoshi, Y., & Jaiser, R. (2019).  
699 Weak Stratospheric Polar Vortex Events Modulated by the Arctic Sea-Ice Loss. *Journal of*  
700 *Geophysical Research: Atmospheres*, 124(2), 858-869. <https://doi.org/10.1029/2018JD029222>.  
701 <https://doi.org/10.1029/2018JD029222>  
702  
703 Hurwitz, M. M., P. A. Newman, and C. I. Garfinkel, 2012: On the influence of North Pacific sea  
704 surface temperature on the Arctic winter climate. *J. Geophys. Res.*, 117, D19110,  
705 doi:10.1029/2012JD017819.  
706  
707 IPCC, 2021: Climate Change 2021: The Physical Science Basis. Contribution of Working Group  
708 I to the Sixth Assessment Report of the Intergovernmental Panel on Climate Change [Masson-  
709 Delmotte, V., P. Zhai, A. Pirani, S.L. Connors, C. Péan, S. Berger, N. Caud, Y. Chen, L.  
710 Goldfarb, M.I. Gomis, M. Huang, K. Leitzell, E. Lonnoy, J.B.R.  
711 Matthews, T.K. Maycock, T. Waterfield, O. Yelekçi, R. Yu, and B. Zhou (eds.)]. Cambridge  
712 University Press. In Press  
713  
714 Jiang, W., Gastineau, G., & Codron, F. (2021). Multicentennial variability driven by salinity  
715 exchanges between the Atlantic and the arctic ocean in a coupled climate model. *Journal of*  
716 *Advances in Modeling Earth Systems*, 13, e2020MS002366.  
717 <https://doi.org/10.1029/2020MS002366>  
718  
719 Kren, A. C., Marsh, D. R., Smith, A. K., & Pilewskie, P. (2016). Wintertime Northern Hemisphere  
720 Response in the Stratosphere to the Pacific Decadal Oscillation Using the Whole Atmosphere  
721 Community Climate Model, *Journal of Climate*, 29(3), 1031-1049. Retrieved Jan 31, 2022, from  
722 <https://journals.ametsoc.org/view/journals/clim/29/3/jcli-d-15-0176.1.xml>  
723  
724 Kidston, J., Scaife, A. A., Hardiman, S. C., Mitchell, D. M., Butchart, N., Baldwin, M. P., & Gray,  
725 L. J., 2015 : Stratospheric influence on tropospheric jet streams, storm tracks and surface  
726 weather. *Nature Geoscience*, 8(6), 433, [doi.org/10.1038/ngeo2424](https://doi.org/10.1038/ngeo2424)  
727  
728 King, M. P., Hell, M., & Keenlyside, N. (2016). Investigation of the atmospheric mechanisms  
729 related to the autumn sea-ice and winter circulation link in the Northern Hemisphere. *Climate*  
730 *dynamics*, 46(3-4), 1185-1195.  
731



- 732 Kim, B. M., Son, S. W., Min, S. K., Jeong, J. H., Kim, S. J., Zhang, X., ... & Yoon, J. H. (2014).  
733 Weakening of the stratospheric polar vortex by Arctic sea-ice loss. *Nature communications*,  
734 5(1), 1-8.  
735
- 736 Kretschmer, M., Coumou, D., Donges, J. F., & Runge, J. (2016). Using causal effect networks to  
737 analyze different Arctic drivers of midlatitude winter circulation. *Journal of Climate*, 29(11), 4069-  
738 4081.
- 739 Labe, Z., Peings, Y., & Magnusdottir, G. (2019). The effect of QBO phase on the atmospheric  
740 response to projected Arctic sea ice loss in early winter. *Geophysical Research Letters*, 46(13),  
741 7663-7671.  
742
- 743 Lang, A., S. Yang, and E. Kaas (2017), Sea ice thickness and recent Arctic  
744 warming, *Geophys. Res. Lett.*, 44, 409–418, doi:10.1002/2016GL071274  
745
- 746 Levine, X.J., Cvijanovic, I., Ortega, P. *et al.* Atmospheric feedback explains disparate climate  
747 response to regional Arctic sea-ice loss. *npj Clim Atmos Sci* 4, 28 (2021).  
748 <https://doi.org/10.1038/s41612-021-00183-w>  
749
- 750 Li, F., Orsolini, Y. J., Wang, H., Gao, Y., & He, S. (2018). Atlantic multidecadal oscillation  
751 modulates the impacts of Arctic sea ice decline. *Geophysical Research Letters*, 45(5), 2497-  
752 2506.  
753
- 754 Liang, Y. C., Frankignoul, C., Kwon, Y. O., Gastineau, G., Manzini, E., Danabasoglu, G., ... &  
755 Zhang, Y. (2021). Impacts of Arctic Sea Ice on Cold Season Atmospheric Variability and Trends  
756 Estimated from Observations and a Multimodel Large Ensemble. *Journal of Climate*, 34(20),  
757 8419-8443.  
758
- 759 Lique, C., Johnson, H. L., & Plancherel, Y. (2018). Emergence of deep convection in the Arctic  
760 Ocean under a warming climate. *Climate dynamics*, 50(9-10), 3833-3847.  
761
- 762 Liu, W., & Fedorov, A. V. (2019). Global impacts of Arctic sea-ice loss mediated by the Atlantic  
763 meridional overturning circulation. *Geophysical Research Letters*, 46(2), 944-952.  
764
- 765 Madec, G., Bourdallé-Badie, R., Bouttier, P. A., Bricaud, C., Bruciaferri, D., Calvert, D., ... &  
766 Vancoppenolle, M. (2017). NEMO ocean engine.  
767
- 768 Mantua, N. J., Hare, S. R., Zhang, Y., Wallace, J. M., & Francis, R. C. (1997). A Pacific  
769 interdecadal climate oscillation with impacts on salmon production. *Bulletin of the American*  
770 *Meteorological Society*, 78(6), 1069-1080.  
771
- 772 Mantua, N. J., & Hare, S. R. (2002). The Pacific decadal oscillation. *Journal of oceanography*,  
773 58(1), 35-44.  
774



775 Manzini, E., Giorgetta, M. A., Esch, M., Kornblueh, L., & Roeckner, E. (2006). The influence of  
776 sea surface temperatures on the northern winter stratosphere: Ensemble simulations with the  
777 MAECHAM5 model. *Journal of Climate*, 19(16), 3863–3881.  
778  
779  
780 Nakamura, H., & Honda, M. (2002). Interannual seesaw between the Aleutian and Icelandic  
781 lows Part III: Its influence upon the stratospheric variability. *Journal of the Meteorological*  
782 *Society of Japan. Ser. II*, 80(4B), 1051-1067.  
783  
784 Newman, M., Alexander, M. A., Ault, T. R., Cobb, K. M., Deser, C., Di Lorenzo, E., ... & Smith,  
785 C. A. (2016). The Pacific decadal oscillation, revisited. *Journal of Climate*, 29(12), 4399-4427.  
786  
787 Ogawa, F., and co-authors, 2018 : Evaluating impacts of recent sea ice loss on the northern  
788 hemisphere winter climate change. *Geophys. Res. Lett.*, 45, 3255–3263. [https://](https://doi.org/10.1002/2017GL076502)  
789 [doi.org/10.1002/2017GL076502](https://doi.org/10.1002/2017GL076502).  
790  
791 Osborne, J. M., Screen, J. A., & Collins, M. (2017). Ocean–atmosphere state dependence of the  
792 atmospheric response to Arctic sea ice loss. *Journal of Climate*, 30(5), 1537-1552.  
793  
794 Park, H. J., & Ahn, J. B. (2016). Combined effect of the Arctic Oscillation and the Western  
795 Pacific pattern on East Asia winter temperature. *Climate Dynamics*, 46(9), 3205-3221  
796  
797 Peings, Y. and G. Magnusdottir, 2014: Response of the wintertime Northern Hemispheric  
798 atmospheric circulation to current and projected Arctic sea ice decline: a numerical study with  
799 CAM5, *J. Climate*, 27, 244–264, 2014 [doi.org/10.1175/JCLI-D-13-00272.1](https://doi.org/10.1175/JCLI-D-13-00272.1)  
800  
801 Peings, Y., Labe, Z. M., & Magnusdottir, G. (2021). Are 100 ensemble members enough to  
802 capture the remote atmospheric response to + 2° C Arctic sea ice loss?. *Journal of Climate*,  
803 34(10), 3751-3769.  
804  
805 Rousset, C., Vancoppenolle, M., Madec, G., Fichefet, T., Flavoni, S., Barthélemy, A., ... &  
806 Vivier, F. (2015). The Louvain-La-Neuve sea ice model LIM3. 6: global and regional capabilities.  
807 *Geoscientific Model Development*, 8(10), 2991-3005.  
808 SIMIP Community (2020). Arctic sea ice in CMIP6. *Geophysical Research Letters*, 47,  
809 e2019GL086749. <https://doi.org/10.1029/2019GL086749>  
810  
811 Sheffield, J., Camargo, S. J., Fu, R., Hu, Q., Jiang, X., Johnson, N., Karnauskas, K. B., Kim, S.  
812 T., Kinter, J., Kumar, S., Langenbrunner, B., Maloney, E., Mariotti, A., Meyerson, J. E., Neelin,  
813 J. D., Nigam, S., Pan, Z., Ruiz-Barradas, A., Seager, R., Serra, Y. L., Sun, D., Wang, C., Xie,  
814 S., Yu, J., Zhang, T., & Zhao, M. (2013). North American Climate in CMIP5 Experiments. Part II:  
815 Evaluation of Historical Simulations of Intraseasonal to Decadal Variability, *Journal of Climate*,  
816 26(23), 9247-9290.  
817



- 818 Screen JA, Simmonds I, 2013: Exploring links between Arctic amplification and mid-latitude  
819 weather. *Geophys Res Lett.* 40,959-964, doi:10.1002/grl.50174.  
820
- 821 Screen, J. A., Deser, C., Simmonds, I., & Tomas, R. (2014). Atmospheric impacts of Arctic sea-  
822 ice loss, 1979–2009: Separating forced change from atmospheric internal variability. *Climate*  
823 *dynamics*, 43(1-2), 333-344.  
824
- 825 Screen, J. A., & Francis, J. A. (2016). Contribution of sea-ice loss to Arctic amplification is  
826 regulated by Pacific Ocean decadal variability. *Nature Climate Change*, 6(9), 856-860.  
827
- 828 Screen, J. A., 2017: Simulated atmospheric response to regional and pan-Arctic sea ice loss, J.  
829 *Climate*, 30, 3945-3962 doi.org/10.1175/JCLI-D-16-0197.1  
830
- 831 Screen, J. A., Deser, C., Smith, D. M., Zhang, X., Blackport, R., Kushner, P. J., ... & Sun, L.  
832 (2018). Consistency and discrepancy in the atmospheric response to Arctic sea-ice loss across  
833 climate models. *Nature Geoscience*, 11(3), 155.  
834
- 835 Screen, J. A., & Deser, C. (2019). Pacific Ocean variability influences the time of emergence of  
836 a seasonally ice-free Arctic Ocean. *Geophysical Research Letters*, 46(4), 2222-2231.  
837
- 838 Seidenglanz, A., Athanasiadis, P., Ruggieri, P., Cvijanovic, I., Li, C., & Gualdi, S. (2021). Pacific  
839 circulation response to eastern Arctic sea ice reduction in seasonal forecast simulations.  
840 *Climate Dynamics*, 1-14.  
841
- 842 Sévellec, F., Fedorov, A. V., & Liu, W. (2017). Arctic sea-ice decline weakens the Atlantic  
843 meridional overturning circulation. *Nature Climate Change*, 7(8), 604.  
844
- 845 Simon, A., Frankignoul, C., Gastineau, G., & Kwon, Y. O. (2020). An Observational Estimate of  
846 the Direct Response of the Cold-Season Atmospheric Circulation to the Arctic Sea Ice Loss.  
847 *Journal of Climate*, 33(9), 3863-3882.  
848
- 849 Simon, A., Gastineau, G., Frankignoul, C., Rousset, C., & Codron, F. (2021). Transient climate  
850 response to Arctic sea-ice loss with two ice-constraining methods. *Journal of Climate*, 1-50.  
851
- 852 Smith, D. M., Screen, J. A., Deser, C., Cohen, J., Fyfe, J. C., García-Serrano, J., ... & Zhang, X.  
853 (2019). The Polar Amplification Model Intercomparison Project (PAMIP) contribution to CMIP6:  
854 Investigating the causes and consequences of polar amplification. *Geoscientific Model*  
855 *Development*, 12(3), 1139-1164.  
856
- 857 Smith, D. M., Eade, R., Andrews, M. B., Ayres, H., Clark, A., Chripko, S., ... & Walsh, A. (2022).  
858 Robust but weak winter atmospheric circulation response to future Arctic sea ice loss. *Nature*  
859 *Communications*, 13(1), 1-15.  
860



861 Sun, L., C. Deser and R. A. Tomas, 2015: Mechanisms of stratospheric and tropospheric  
862 circulation response to projected Arctic sea ice loss. *J. Climate*, 28, 7824-7845, doi:  
863 10.1175/JCLI-D-15-0169.1.  
864  
865 Trenberth, K. E., & Hurrell, J. W. (1994). Decadal atmosphere-ocean variations in the Pacific.  
866 *Climate Dynamics*, 9(6), 303-319.  
867  
868 Trenberth, K. E., Branstator, G. W., Karoly, D., Kumar, A., Lau, N. C., & Ropelewski, C. (1998).  
869 Progress during TOGA in understanding and modeling global teleconnections associated with  
870 tropical sea surface temperatures. *Journal of Geophysical Research: Oceans*, 103(C7), 14291-  
871 14324.  
872  
873 Vancoppenolle, M., Fichet, T., Goosse, H., Bouillon, S., Madec, G., & Maqueda, M. A. M.  
874 (2009). Simulating the mass balance and salinity of Arctic and Antarctic sea ice. 1. Model  
875 description and validation. *Ocean Modelling*, 27(1-2), 33-53.  
876  
877 Wilks, D. (2016). "The stippling shows statistically significant grid points": How research results  
878 are routinely overstated and overinterpreted, and what to do about it. *Bulletin of the American*  
879 *Meteorological Society*, 97(12), 2263-2273.  
880  
881 Woo, S. H., Sung, M. K., Son, S. W., & Kug, J. S. (2015). Connection between weak  
882 stratospheric vortex events and the Pacific decadal oscillation. *Climate dynamics*, 45(11), 3481-  
883 3492.  
884  
885 Zhang, J., Tian, W., Chipperfield, M. P., Xie, F., & Huang, J. (2016). Persistent shift of the Arctic  
886 polar vortex towards the Eurasian continent in recent decades. *Nature Climate Change*, 6(12),  
887 1094-1099.  
888  
889  
890  
891  
892  
893  
894  
895  
896  
897  
898  
899  
900  
901  
902  
903  
904